NANO LETTERS

Letter

pubs.acs.org/NanoLett

Atomic-Scale Mechanisms of Defect-Induced Retention Failure in Ferroelectrics

Linze Li,[†] Yi Zhang,[†] Lin Xie,[†,‡] Jacob R. Jokisaari,[§] Christianne Beekman,[∥] Jan-Chi Yang,[⊥] Ying-Hao Chu,[#] Hans M. Christen,[∞] and Xiaoqing Pan*[,†,▽]

[†]Department of Chemical Engineering and Materials Science, University of California - Irvine, Irvine, California 92697, United States

[‡]National Laboratory of Solid State Microstructures and College of Engineering and Applied Sciences, Nanjing University, Nanjing, Jiangsu 210093, China

[§]Department of Materials Science and Engineering, University of Michigan, Ann Arbor, Michigan 48109, United States

[∥]Materials Science and Technology Division, Oak Ridge National Laboratory, Oak Ridge, Tennessee 37831, United States

[⊥]Department of Physics, National Cheng Kung University, Tainan 701, Taiwan

[#]Department of Materials Science and Engineering, National Chiao Tung University, Hsinchu 300, Taiwan

[∞]Center for Nanophase Materials Sciences, Oak Ridge National Laboratory, Oak Ridge, Tennessee 37831, United States

[▽]Department of Physics and Astronomy, University of California - Irvine, Irvine, California 92697, United States

Supporting Information

ABSTRACT: The ability to switch the ferroelectric polarization using an electric field makes ferroelectrics attractive for application in nanodevices such as high-density memories. One of the major challenges impeding this application, however, has been known as "retention failure", which is a spontaneous process of polarization back-switching that can lead to data loss. This process is generally thought to be caused by the domain instability arising from interface boundary conditions and countered by defects, which can pin the domain wall and impede the back-switching. Here, using in situ transmission electron microscopy and atomic-scale scanning transmission electron microscopy, we show that the polarization retention failure can be induced by commonly observed nanoscale impurity defects in $BiFeO_3$ thin films. The interaction between polarization and the defects can also lead to the stabilization of novel functional nanodomains with mixed-phase structures and head-to-head polarization configurations. Thus, defect engineering provides a new route for tuning properties of ferroelectric nanosystems.

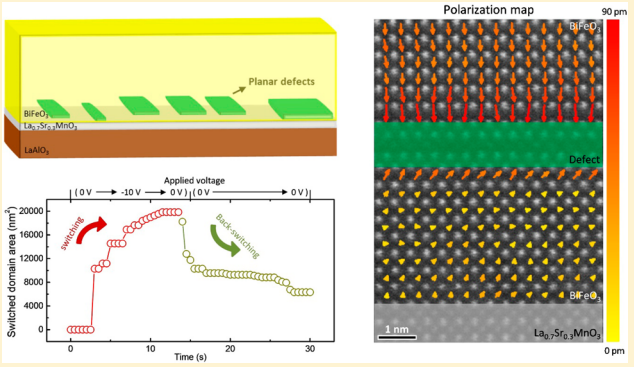

KEYWORDS: *Ferroelectric, retention failure, defect, mixed-phase structure, head-to-head polarization*

A ferroelectric is generally defined as a material whose spontaneous polarization can be reversed through the application of an external electric field that is greater than the coercive field, a behavior similar to the reorientation of magnetic moments under an applied magnetic field for ferromagnetic materials. Despite having been studied for around a century, ferroelectrics have gained increasing attention over the past decade, because recent advances in atomic-level control of thin-film growth have made it possible to epitaxially grow high-quality ferroelectric thin films on a large variety of single crystal substrates with precise control over composition, atomic arrangements, and interfaces.[1−5] The availability of such films provides unprecedented opportunities to design, tailor and examine their physical properties; numerous studies have revealed that the switchable polarization can couple with other physical parameters such as electronic transport properties,[6−8] photovoltaic properties,[9,10] strain,[11] magnetic order,[12] or surface chemistry.[13] Ferroelectric materials, then, find potential applications in high-density memories and a broad range of electronic, magnetoelectric, photoelectric, and electromechanical applications.

A long-standing issue that has to be resolved in order to realize ferroelectric applications has been that the switched polarization is sometimes unstable and can relax to its original state through a spontaneous process of polarization back-switching. Such process, known as "retention failure", can lead to a loss of stored information in ferroelectric memories and disable functionalities coupled with the switched polarization in

Received: February 16, 2017
Revised: April 12, 2017
Published: May 4, 2017

DOI: 10.1021/acs.nanolett.7b00696
Nano Lett. 2017, 17, 3556−3562

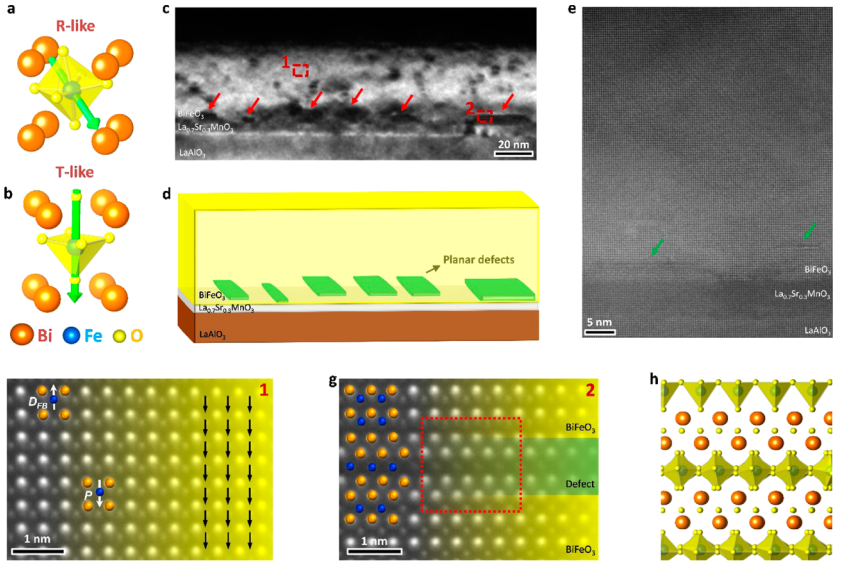

Figure 1. (a,b) Atomic models of the pseudocubic structures of *R*-like and *T*-like $BiFeO_3$. Polarizations are shown by light green arrows. (c) Cross-sectional dark-field TEM image showing an array of planar defects just above the $BiFeO_3/La_{0.7}Sr_{0.3}MnO_3$ interface. The defects are indicated by the red arrows. (d) Schematic of the heterostructure in (c). (e) A HAADF STEM image of the $BiFeO_3/La_{0.7}Sr_{0.3}MnO_3/LaAlO_3$ structure. Planar defects are indicated by the green arrows, and no dislocations are observed at the interfaces. (f,g) Averaged HAADF STEM images of the two different regions highlighted by the rectangles in (c). The overlaid brown and blue balls mark the Bi and Fe atom columns, respectively. The black arrows in (f) indicate a uniform downward polarization. (h) Atomic model of the defect highlighted by the rectangle in (g).

multifunctional applications. This process is tied to an asymmetric free-energy landscape between the two opposite polarization states. Specifically, the polarization orientations are not degenerate and the written polarization has higher energy than the other polarization state, leading to a gradual transition to the lower energy state. It has been generally accepted that the electrostatic boundary condition correlated to the properties of ferroelectric/electrode interfaces is the primary origin for the nondegenerate polarization states. For instance, strong depolarization fields can arise at uncompensated interfaces where interfacial dead-layer or nonswitchable layers exist[14−16] and the semiconductor/metal contact at the ferroelectric/electrode interface can generate a Schottky built-in field.[17] An imbalance between the electrostatic boundary conditions at the two interfaces of a ferroelectric film can impose a net effective field, triggering polarization back-switching. Elastic boundary conditions, that is, the substrate-induced strain, can also affect the domain stability. For example, it has been suggested that the depolarization field and the Schottky built-in field at the ferroelectric/electrode interface could be strain-dependent.[18] Furthermore, the substrate-induced strain may be gradually released in ferroelectric films through the formation of dislocations, resulting in a strain gradient. Such a strain gradient can produce an effective built-in field through flexoelectric effects and therefore can also alter the domain stability.[19]

On the other hand, defects were often thought to counter the process of retention failure by acting as pinning centers hindering the domain wall motion. Previous experimental results have shown that domain walls can be pinned by vacancies,[20,21] dislocations,[22] phase boundaries,[23] or pre-existing ferroelastic domains,[24] all of which would enhance the stability of written domains. However, another major type of defects, impurity defects with structures different from the host materials, were usually overlooked. These defects are often buried in the bulk material and can be atomically thin in dimension, making their characterization quite demanding using conventional surface probes such as piezoresponse force microscopy (PFM). Recent transmission electron microscopy (TEM) studies, however, have revealed the common occurrence of such impurity defects in ferroelectric oxides,[25−27] and these defects may modify ferroelectric properties. Here, using atomic-scale scanning transmission electron microscopy (STEM) and in situ TEM,[28] we directly resolve atomic structures and domain switching in $BiFeO_3$ thin films where arrays of planar impurity defects are located just above the substrate interfaces. We show that the impurity defects can induce strong built-in field, which not only leads to mixed-phase structures with head-to-head polarization configuration and polarization enhancement, but also can destabilize written domains. These defects could thus play a dominant role in the control of ferroelectric properties.

$BiFeO_3$ is a room-temperature multiferroic exhibiting coupled ferroelectric (T_C ∼ 1103 K) and antiferromagnetic (T_N ∼ 650 K) order.[29,30] Its bulk crystal has a rhombohedral structure, which can also be envisioned as two pseudocubic (PC) perovskite unit cells connected along the body diagonal with the two oxygen octahedra in the connected perovskite units rotated clockwise and counterclockwise around this axis by 13.8°.[30] Structures of epitaxial $BiFeO_3$ films with tensile or moderate compressive (<∼4.5%) misfit strain imposed by underlying substrates are monoclinically distorted but closely resemble the bulk rhombohedral phase and are therefore usually referred to as "rhombohedral-like (*R*-like)" structures.[31] In pseudocubic unit cells of the *R*-like structure (Figure 1a), the oxygen octahedra and the central Fe cation are displaced from their respective positions at the face and body centers, giving rise to a large spontaneous polarization (∼100 $\mu C\ cm^{-2}$) along the $\langle 111\rangle_{PC}$ directions. Under a large compressive epitaxial strain exceeding ∼4.5%, $BiFeO_3$ can also be stabilized into a monoclinic structure that is "tetragonal-like" (*T*-like).[31] In the *T*-like structure (Figure 1b), the Fe atom is five-coordinated,

DOI: 10.1021/acs.nanolett.7b00696
Nano Lett. 2017, 17, 3556−3562

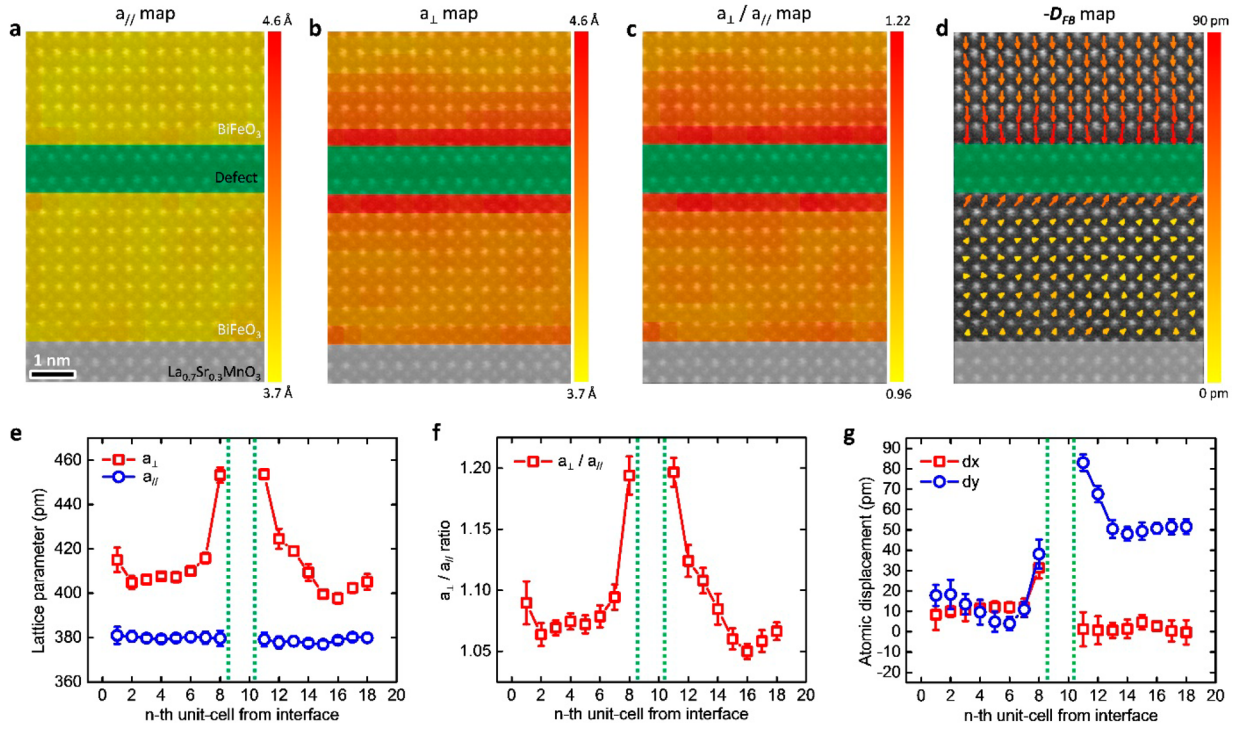

Figure 2. (a–d) Color maps of (a) the in-plane lattice parameter $a_{//}$, (b) the out-of-plane lattice parameter $a_{\perp}$, (c) the $a_{\perp}/a_{//}$ ratio, and (d) spatial distribution of the $-\mathbf{D}_{FB}$ vectors overlaid on the same HAADF STEM image in which one planar defect is located above the $BiFeO_3/La_{0.7}Sr_{0.3}MnO_3$ interface. The defect and the $La_{0.7}Sr_{0.3}MnO_3$ substrate are overlaid with uniform green and silver colors, respectively. (e–g) The $a_{//}$, $a_{\perp}$, $a_{\perp}/a_{//}$ and $-\mathbf{D}_{FB}$ changes in the $BiFeO_3$ lattice across the defect. The green dashed lines mark the position of the defect. In (g), d*x* and d*y* represents the magnitude of the horizontal and vertical components of the $-\mathbf{D}_{FB}$ vector.

forming an oxygen square-pyramidal that is displaced from the center of the pseudocubic unit cell. This gives rise to a large polarization (~150 $\mu C/cm^2$) oriented along the out-of-plane direction.

In this work, 50 nm thick epitaxial $BiFeO_3$ thin films with 8 nm $La_{0.7}Sr_{0.3}MnO_3$ buffered electrodes were grown on $LaAlO_3$ single crystal substrates by pulsed-laser deposition as described previously.[32] Typical mixed-phase structures containing stripe patterns driven by the large epitaxial strain (~4.5%) were observed in the $BiFeO_3$ films[33] (Figure S1). While early work ascribed these patterns to stripes of *R*-like domains embedded into *T*-like matrix, it is now understood that the stripes are triclinic polymorphs, referred to as the *S*′ phase.[34] This *S*′ phase is energetically close to the *T*-like phase but structurally similar to the *R*-like phase.[34] Independent of this stripe behavior, this work focuses on local regions within the *T*-like matrix, where we find arrays of planar defects with a length of 5–30 nm just above the interfaces (Figure 1c–e)

The atomic-level structure of the $BiFeO_3$ thin films was characterized by aberration-corrected high-angle annular dark-field (HAADF) STEM imaging. In a HAADF image of the *T*-like $BiFeO_3$ lattice shown in Figure 1f, the Bi columns appear as the brighter dots, the Fe columns show weaker contrast, and the oxygen atoms are not visible. Using the HAADF image, the position of each atom-column can be measured by fitting the atomic columns as two-dimensional (2D) Gaussian peaks.[35,36] On the basis of the measured positions, the strain distribution within the $BiFeO_3$ lattice can be directly mapped by calculating the lattice parameters. A vector in the image plane, $\mathbf{D}_{FB}$, can be defined as the atomic displacement of the Fe cation from the center of the unit cell formed by its four Bi neighbors.[35,36] This $\mathbf{D}_{FB}$ vector, as the dominant manifestation of the ferroelectric polarization in $BiFeO_3$, points toward the center of the negative oxygen charges and thus is exactly opposite to the polarization component in the image plane. Therefore, $-\mathbf{D}_{FB}$ vectors can be used to estimate the polarization and are called polarization vectors. Our measurements show that the out-of-plane lattice parameter ($a_{\perp}$) over the in-plane lattice parameter ($a_{//}$) ratio is ~1.06 for the majority of the films, which is much smaller than the value of ~1.25 measured by X-ray diffraction in the bulk films of *T*-like $BiFeO_3$ grown on $LaAlO_3$ substrates,[31] suggesting a possible structural relaxation in the TEM specimen.[37] Nevertheless, mapping of the polarization vectors confirms that the majority phase is still *T*-like, because the polarization in most regions is oriented along the $[00\bar{1}]_{PC}$ direction, with the exception of some interfacial regions below the defects as we will discuss later.

A HAADF image of a region containing a planar defect in the $BiFeO_3$ matrix is shown in Figure 1g. As there are no other elements introduced during film growth, the defect should also be composed of Bi, Fe, and O atoms, with the brighter dots in the HAADF image corresponding to the heavier Bi columns, the weaker dots corresponding to the lighter Fe columns, while O columns are not visible. The arrangements of Bi and Fe atoms within the defect closely resemble those in the Aurivillius phase materials, for example, Bi_2WO_6, which is built by alternating layers of Bi_2O_2 and pseudoperovskite blocks.[38] Examining the defect, a form of Bi_2FeO_{6-x}, composed of a single layer of FeO_6 octahedra sandwiched between two Bi_2O_2 layers as shown in Figure 1h is reasonable, though the exact stoichiometry of oxygen and the precise positions of oxygen atoms may differ. Formation of Bismuth-rich regions may indeed be favored by the Bismuth-rich growth environment, and the exact extent of these features is expected to depend

DOI: 10.1021/acs.nanolett.7b00696
Nano Lett. 2017, 17, 3556–3562

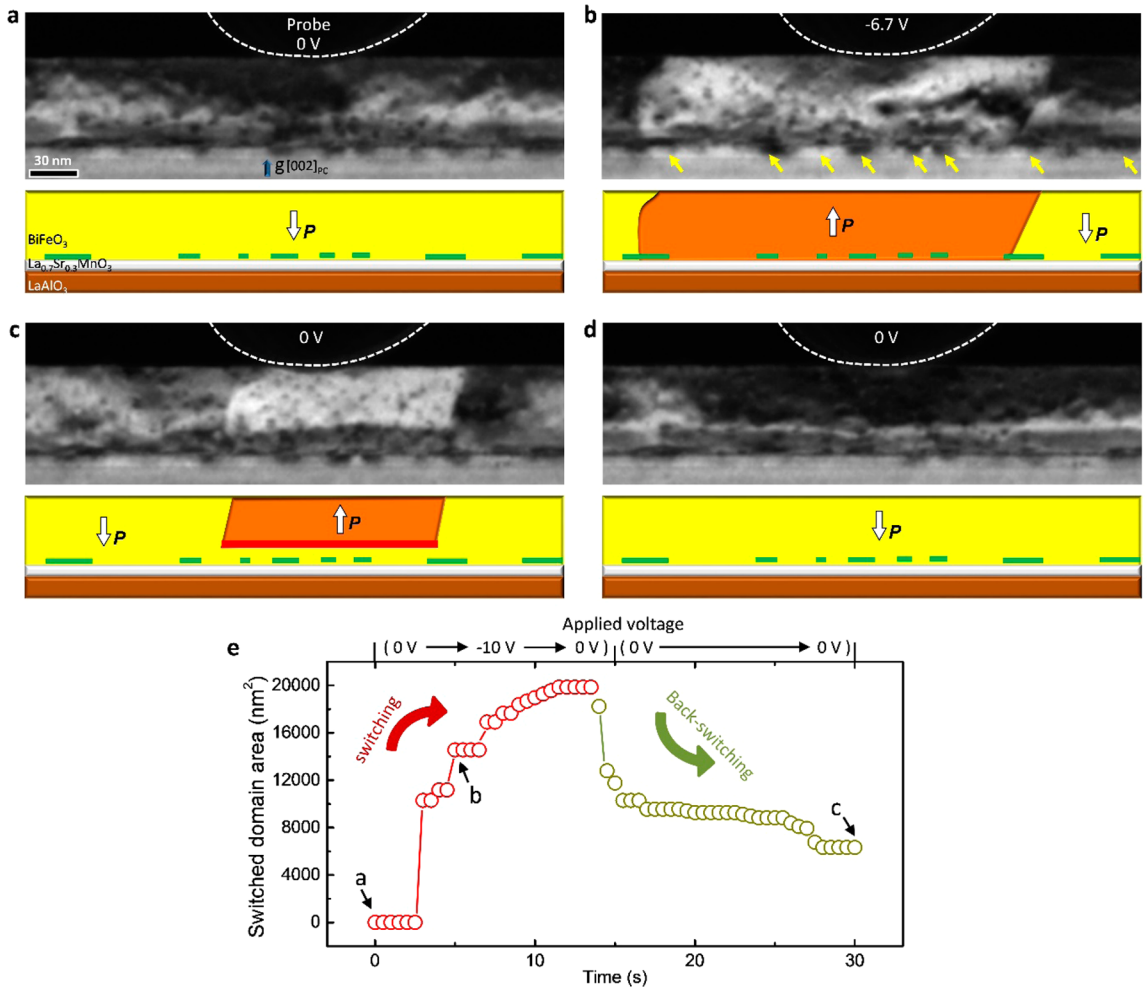

Figure 3. (a–d) Chronological TEM dark-field image series and corresponding schematics depicting the evolution of an upward polarized domain from a downward polarized matrix: (a) the original state, (b) switched domain under an applied voltage, (c) metastable domain state at 15 s after the voltage was removed, and (d) final stable state at 20 min after the voltage was removed. An array of planar defects at the $BiFeO_3/La_{0.7}Sr_{0.3}MnO_3$ interface are indicated by the yellow arrows in (b) and are shown by the green lines in the schematics. In (c), a horizontal tail-to-tail charged domain wall is marked by the red line in the schematic. (e) Plot of the measured area of the switched domain as a function of time (bottom axis) and applied voltage (top axis). The locations of (a–c) are marked.

significantly on growth rate and growth temperature. The same-type of Bi_2FeO_{6-x} impurity phase has also been observed in a previous study of $BiFeO_3$ thin films grown on $TbScO_3$ or on $SrTiO_3$ substrates. Their observations show much larger regions of the impurity phase, forming nanoparticles or nanopillars embedded in the $BiFeO_3$ matrix with a feature size of tens of nanometers.[25] In comparison, the impurity planar defects observed here are only a few atomic layers in thickness and perfectly epitaxial along the film grown direction. Furthermore, our observations also suggest that the impurity structures may adopt smaller dimensions, forming point defects in the thin films (Figure S2).

The strain and polarization distribution in the $BiFeO_3$ lattice adjacent to the planar defect was determined by mapping of the lattice parameters (Figure 2a–c) and the polarization vectors (Figure 2d). By averaging the data from each lattice layer, the change of the lattice parameters and the magnitude of the polarization vectors in the $BiFeO_3$ lattice across the defect can be plotted in Figure 2e–g. The strain mapping results shows that whereas $a_{//}$ remains almost constant in the examined region (Figure 2a,e), a sharp increase of $a_{\perp}$ occurred in the lattice layers that are in contact with the defect (Figure 2b,e), resulting in a local high $a_{\perp}/a_{//}$ ratio of ~1.20 (Figure 2c,f). Such change of $a_{\perp}$ could be induced by the out-of-plane lattice mismatch between $BiFeO_3$ and the defect. Specifically, the defect with a thickness of 10.2 Å is inserted into the $BiFeO_3$ lattice, replacing three pseudocubic unit cells with a thickness of 12.1 Å (Figure S3); this would induce the out-of-plane lattice expansion in the neighboring $BiFeO_3$ layers. Furthermore, there also exists large strain gradients along the out-of-plane direction, as the $a_{\perp}/a_{//}$ ratio relaxes to the bulk value (~1.06) within several unit cells near the defect.

The map of the polarization vectors surrounding the planar defect generally shows a head-to-head polarization configuration (Figure 2d). An enhancement in the magnitude of the polarization was also observed in the $BiFeO_3$ lattice in contact with the defect (Figure 2g), which is clearly coupled to the local increase in tetragonality, that is, the enhanced $a_{\perp}/a_{//}$ ratio in these layers. Furthermore, the polarization map shows an interesting change in the $BiFeO_3$ lattice symmetry in the two regions separated by the defect (Figure 2d). While the lattice above the defect possesses a *T*-like structure with polarization oriented along $[00\bar{1}]_{PC}$ direction, the lattice below the defect is possibly in the *S′* (or *R*-like) phase, with mostly attenuated

DOI: 10.1021/acs.nanolett.7b00696
Nano Lett. 2017, 17, 3556–3562

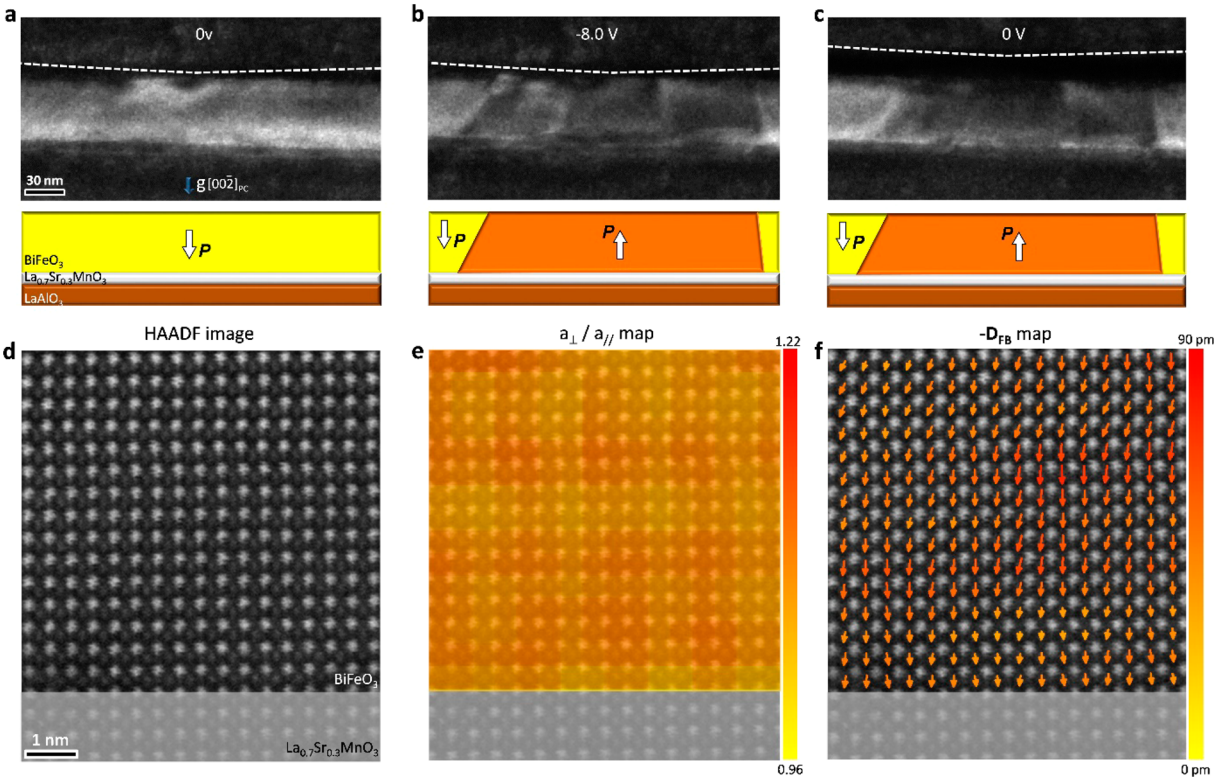

Figure 4. (a–c) Chronological TEM dark-field image series depicting the creation and stabilization of an upward polarized domain in a local $BiFeO_3$ film without planar impurity defects. (d) A HAADF STEM image showing the $BiFeO_3/La_{0.7}Sr_{0.3}MnO_3$ interfacial region of the local film. (e) Color map of the $a_\perp/a_{//}$ ratio and (f) spatial distribution of the $-\mathbf{D}_{FB}$ vectors overlaid on the same HAADF STEM image.

polarization oriented along the diagonal, pointing upward in the image plane. Such mixed-phase structures can be associated with the defect. As a previous study has shown, Bi_2O_2 layers existing at the substrate interfaces can induce the formation of *T*-like structures in moderately strained (~1.5%) $BiFeO_3$ films grown on $SrTiO_3$ substrates,[39] the Bi_2O_2 layers within the defect observed here could also be the origin for the stabilization of the *T*-like phase above the local *S*′ (or *R*-like) structures. On the other hand, the upward polarization below the defect is opposed to the downward polarization enforced by the built-in field at the Schottky contact of the $BiFeO_3/La_{0.7}Sr_{0.3}MnO_3$ (n-type-semiconductor/metal) interface.[40] This suggests that a strong built-in field pointing toward the defect exists and this field can flip the polarization adjacent to the defect. The stabilized upward polarization below the defect is further suppressed by the downward Schottky built-in field from the back electrode, resulting in the observed *S*′ (or *R*-like) phase with attenuated polarization.

A local domain switching event in the presence of an array of planar defects just above the $BiFeO_3/La_{0.7}Sr_{0.3}MnO_3$ interface was captured by in situ TEM (Figure 3). A bias was applied between a tungsten surface probe and the $La_{0.7}Sr_{0.3}MnO_3$ bottom electrode and was linearly changed from 0 to −10.0 V and then back to 0 V over 15 s. The film was originally in a *T*-like downward polarization (Figure 3a). Note that the image contrast here is also affected by the film bending caused by the applied force from the surface probe, which leads to some bright/dark contrast in the image of the film where all the polarization is pointing down. The switching event shows that, although a large domain with upward polarization can be created with an applied voltage (Figure 3b), the created domain shrank back to a smaller metastable state in 15 s after the voltage was removed (Figure 3c). While the switched domain under the applied voltage (Figure 3b) penetrated across the whole film thickness, the metastable domain after the removal of the applied voltage (Figure 3c) only penetrated from the top surface to about 35 nm in depth, resulting the formation of a horizontal tail-to-tail charged domain wall at the middle of the film. This suggests that, at this stage, a spontaneous back-switching only occurred at a thin sublayer above the $BiFeO_3/La_{0.7}Sr_{0.3}MnO_3$ interface. A plot of the area of the switched domain measured from the TEM images as a function of time and applied voltage, in Figure 3e, shows that the domain switching induced by the applied bias is affected by several pinning and field-assisted unpinning of domain walls, where the domain area remained constant until the applied voltage was large enough to trigger a sudden expansion in area. Such a domain wall pinning effect is further evidenced by the fact that the boundaries of the switched domain were not in the low-energy vertical orientation and instead presented inclined or curved configurations (Figure 3b,c). Possible pinning centers could be the point impurity defects randomly distributed in the thin film (Figure S2) or oxygen vacancies that commonly exist in ferroelectric oxides. Right before the applied voltage went to zero (Figure. 3e), partial spontaneous back-switching of the written domain occurred via a rapid shrinkage to the metastable state. After the applied voltage went to zero, this metastable state further relaxed to smaller sizes through slow thermodynamic processes, and eventually annihilated in 20 min (Figure 3d). Note that the probe was moved away from the film surface after recording Figure 3c and moved back to the same location before recording Figure 3d, and therefore no force was applied to the film during the 20 min.

DOI: 10.1021/acs.nanolett.7b00696
Nano Lett. 2017, 17, 3556–3562

The most likely cause for the observed retention failure phenomena in these $BiFeO_3$ films is a strong built-in field pointing downward through the film. The built-in field here would be a combination of the Schottky field from the back contact and the downward built-in field induced by the planar defects above them. Note that where the defects are localized, they will locally offset (or cancel, or overwrite) the Schottky field; however, at a distance exceeding the lateral distance between individual defects, only the macroscopically averaged electric field will remain, and this is shown here to be dominated by the planar defects. First, the planar-defect-induced field should be stronger than the Schottky field, as it is large enough to stabilize a polarization opposite to the Schottky field below the defect, forming a head-to-head polarization configuration that is usually considered unstable in ferroelectrics (Figure 2d). Second, as observed in Figure 3c, the early stage of the retention failure was accompanied by back-switching at the interfacial sublayer, suggesting the back-switching was initiated at local nanoregions adjacent to the planar defects. In fact, the defect-induced electric field could be related to the defect-induced strain gradient through the flexoelectric effect. The opposite out-of-plane strain gradients above and below the planar defect lead to head-to-head built-in field pointing to the defect. With the experimentally obtained values of strain gradient (Figure 2), the out-of-plane flexoelectric field, $E_{F,\perp}$, can be estimated using[41]

$$E_{F,\perp} \approx \lambda \frac{e}{\varepsilon_0 a_\perp} \frac{\partial u_\perp}{\partial z} \quad (1)$$

where λ is a scaling factor, e is the electronic charge, $a_\perp$ is the out-of-plane lattice constant, ε_0 is the permittivity of free space, and $\frac{\partial u_\perp}{\partial z}$ is the out-of-plane strain gradient. By assuming $\lambda = 1$,[41] $E_{F,\perp}$ is calculated to be $\sim 3.7 \times 10^3$ MV/m, which is 2 orders of magnitude higher than the typical value of Schottky built-in field at the $BiFeO_3/La_{0.7}Sr_{0.3}MnO_3$ interface.[40] This flexoelectric field can reverse the polarization and induce the observed polarization enhancement.

Furthermore, we found at local regions in the same film where impurity defects were not observed, a switched domain was stable after the removal of the applied voltage (Figure 4a–c). Such stability of the written domain is in agreement with previous observations of ferroelectric switching in similar systems, that is, *T*-like $BiFeO_3$ films grown on $LaAlO_3$ substrates with $La_{0.7}Sr_{0.3}MnO_3$ back electrodes.[42] In these regions without impurity defects, maps of lattice parameters and polarization vectors based on HAADF STEM images show uniform *T*-like domain structures above the interfaces (Figure 4d–f). In regions both with and without impurity defects, the films show good epitaxy at the $BiFeO_3/La_{0.7}Sr_{0.3}MnO_3$ interfaces without dislocations, excluding depolarization effects caused by interfacial nonferroelectric dead-layers[14] or flexoelectric effects induced by strain gradients related to dislocations.[19] Therefore, the existence of the impurity defects should be crucial to the observed domain instability.

As $BiFeO_3$ film growth is very sensitive to the deposition parameters and pure-phase $BiFeO_3$ can only be obtained within narrow parameter combinations,[25] the impurity defects observed in our thin films could be induced by slight stoichiometry fluctuations occurring during the growth, either due to fluctuations of deposition parameters or inhomogeneity of the target. This suggests that, impurity defects, either of the Aurivillius phase or other types of structures, may be common in perovskite thin films. Such defects can strongly interact with the host materials and affect static polarization structures and domain-switching dynamics.

Although these defects may destabilize written domains and would be less useful for ferroelectric memory devices, the finding of defect induced change of polarization structures suggests potential new routes of tuning ferroelectric properties. For example, it may be possible to produce *R*–*T* mixed-phase structures, which are usually correlated to giant piezoelectricity, in low-strain $BiFeO_3$ films by intentionally creating the Bi_2FeO_{6-x} impurity defects into the film matrix. Because the structure below the defect is *R*-like and the structure above the defect is *T*-like, the *R*–*T* ratio of the structures in the film may be tuned if the position of the defect can be controlled. Moreover, head-to-head polarization configurations have previously been extensively studied due to their enhanced electronic properties. A combination of both head-to-head polarization and mixed-phase structures within the single functional unit reported here may lead to novel applications for nanodevices. Engineering defects, therefore, could open new avenues for the control of nanodomain structures and the creation of new polarization states that are not easily accessible through conventional methods.

■ ASSOCIATED CONTENT

Supporting Information

The Supporting Information is available free of charge on the ACS Publications website at DOI: 10.1021/acs.nanolett.7b00696.

Details on experimental methods, including film growth, transmission electron microscopy (TEM), and atomic force microscopy (AFM) (PDF)

■ AUTHOR INFORMATION

Corresponding Author

*E-mail: xiaoqinp@uci.edu.

ORCID

Linze Li: 0000-0001-5362-8991

Ying-Hao Chu: 0000-0002-3435-9084

Xiaoqing Pan: 0000-0002-0965-8568

Present Address

(C.B.) Florida State University Physics Department and National High Magnetic Field Laboratory, Tallahassee, Florida 32310, United States.

Notes

The authors declare no competing financial interest.

■ ACKNOWLEDGMENTS

The work was supported by the Department of Energy (DOE) under Grant DE-SC0014430. It is partially supported by the National Basic Research Program of China (No. 2015CB654901) (L.X.), the National Science Foundation under Grants DMR-1420620 (J.R.J.) and DMR-1506535 (Y.Z.). Film growth at Oak Ridge National Laboratory was supported by DOE Office of Science, Materials Sciences, and Engineering Division. Y.H.C. acknowledges the support of the Ministry of Science and Technology, Taiwan, under Grant MOST 103-2119-M-009-003-MY3. The authors would also like to acknowledge the National Center for Electron Microscopy at Lawrence Berkeley National Laboratory for their support under the DOE Grant DE-AC0205CH11231 for user facilities. X.Q.P.

DOI: 10.1021/acs.nanolett.7b00696
Nano Lett. 2017, 17, 3556–3562

directed this project. L.Z.L. designed and carried out the experiments assisted by Y.Z., L.X., and J.R.J. and performed data analysis. C.B. and J.C.Y. synthesized thin films with direction from H.M.C. and Y.H.C., respectively. All authors discussed the results and contributed to writing the manuscript.

REFERENCES

(1) Wang, J.; Neaton, J. B.; Zheng, H.; Nagarajan, V.; Ogale, S. B.; Liu, B.; Viehland, D.; Vaithyanathan, V.; Schlom, D. G.; Waghmare, U. V.; Spaldin, N. A.; Rabe, K. M.; Wuttig, M.; Ramesh, R. *Science* **2003**, *299* (5613), 1719−1722.

(2) Bark, C. W.; Felker, D. A.; Wang, Y.; Zhang, Y.; Jang, H. W.; Folkman, C. M.; Park, J. W.; Baek, S. H.; Zhou, H.; Fong, D. D.; Pan, X. Q.; Tsymbal, E. Y.; Rzchowski, M. S.; Eom, C. B. *Proc. Natl. Acad. Sci. U. S. A.* **2011**, *108* (12), 4720−4724.

(3) Schlom, D. G.; Chen, L. Q.; Eom, C. B.; Rabe, K. M.; Streiffer, S. K.; Triscone, J. M. *Annu. Rev. Mater. Res.* **2007**, *37*, 589−626.

(4) Schlom, D. G.; Chen, L. Q.; Pan, X. Q.; Schmehl, A.; Zurbuchen, M. A. *J. Am. Ceram. Soc.* **2008**, *91* (8), 2429−2454.

(5) Martin, L. W.; Chu, Y. H.; Ramesh, R. *Mater. Sci. Eng., R* **2010**, *68* (4−6), 89−133.

(6) Garcia, V.; Fusil, S.; Bouzehouane, K.; Enouz-Vedrenne, S.; Mathur, N. D.; Barthelemy, A.; Bibes, M. *Nature* **2009**, *460* (7251), 81−84.

(7) Choi, T.; Lee, S.; Choi, Y. J.; Kiryukhin, V.; Cheong, S. W. *Science* **2009**, *324* (5923), 63−66.

(8) Maksymovych, P.; Jesse, S.; Yu, P.; Ramesh, R.; Baddorf, A. P.; Kalinin, S. V. *Science* **2009**, *324* (5933), 1421−1425.

(9) Ji, W.; Yao, K.; Liang, Y. C. *Adv. Mater.* **2010**, *22* (15), 1763−1766.

(10) Yi, H. T.; Choi, T.; Choi, S. G.; Oh, Y. S.; Cheong, S. W. *Adv. Mater.* **2011**, *23* (30), 3403−3407.

(11) Zhang, J. X.; Xiang, B.; He, Q.; Seidel, J.; Zeches, R. J.; Yu, P.; Yang, S. Y.; Wang, C. H.; Chu, Y. H.; Martin, L. W.; Minor, A. M.; Ramesh, R. *Nat. Nanotechnol.* **2011**, *6* (2), 98−102.

(12) Ramesh, R.; Spaldin, N. A. *Nat. Mater.* **2007**, *6* (1), 21−29.

(13) Wang, R. V.; Fong, D. D.; Jiang, F.; Highland, M. J.; Fuoss, P. H.; Thompson, C.; Kolpak, A. M.; Eastman, J. A.; Streiffer, S. K.; Rappe, A. M.; Stephenson, G. B. *Phys. Rev. Lett.* **2009**, *102* (4), 047601.

(14) Wang, J.; Xia, Y. F.; Chen, L. Q.; Shi, S. Q. *J. Appl. Phys.* **2011**, *110* (11), 114111.

(15) Stengel, M.; Spaldin, N. A. *Nature* **2006**, *443* (7112), 679−682.

(16) Tagantsev, A. K.; Gerra, G. *J. Appl. Phys.* **2006**, *100* (5), 051607.

(17) Dawber, M.; Rabe, K. M.; Scott, J. F. *Rev. Mod. Phys.* **2005**, *77* (4), 1083−1130.

(18) Guo, E. J.; Roth, R.; Das, S.; Herklotz, A.; Dorr, K. *Appl. Phys. Lett.* **2015**, *106* (7), 072904.

(19) Lee, D.; Jeon, B. C.; Yoon, A.; Shin, Y. J.; Lee, M. H.; Song, T. K.; Bu, S. D.; Kim, M.; Chung, J. S.; Yoon, J. G.; Noh, T. W. *Adv. Mater.* **2014**, *26* (29), 5005−5011.

(20) Paruch, P.; Giamarchi, T.; Triscone, J. M. *Phys. Rev. Lett.* **2005**, *94* (19), 197601.

(21) Lubk, A.; Rossell, M. D.; Seidel, J.; He, Q.; Yang, S. Y.; Chu, Y. H.; Ramesh, R.; Hytch, M. J.; Snoeck, E. *Phys. Rev. Lett.* **2012**, *109* (4), 047601.

(22) Vrejoiu, I.; Le Rhun, G.; Zakharov, N. D.; Hesse, D.; Pintilie, L.; Alexe, M. *Philos. Mag.* **2006**, *86* (28), 4477−4486.

(23) Huang, Y. C.; Liu, Y. Y.; Lin, Y. T.; Liu, H. J.; He, Q.; Li, J. Y.; Chen, Y. C.; Chu, Y. H. *Adv. Mater.* **2014**, *26* (36), 6335−6340.

(24) Gao, P.; Britson, J.; Jokisaari, J. R.; Nelson, C. T.; Baek, S. H.; Wang, Y. R.; Eom, C. B.; Chen, L. Q.; Pan, X. Q. *Nat. Commun.* **2013**, *4*, 2791.

(25) Deniz, H.; Bhatnagar, A.; Pippel, E.; Hillebrand, R.; Hahnel, A.; Alexe, M.; Hesse, D. *J. Mater. Sci.* **2014**, *49* (20), 6952−6960.

(26) MacLaren, I.; Wang, L. Q.; Craven, A. J.; Ramasse, Q. M.; Schaffer, B.; Kalantari, K.; Reaney, I. M. *APL Mater.* **2014**, *2* (6), 066106.

(27) MacLaren, I.; Wang, L. Q.; Morris, O.; Craven, A. J.; Stamps, R. L.; Schaffer, B.; Ramasse, Q. M.; Miao, S.; Kalantari, K.; Sterianou, I.; Reaney, I. M. *APL Mater.* **2013**, *1* (2), 021102.

(28) Li, L. Z.; Jokisaari, J. R.; Pan, X. Q. *MRS Bull.* **2015**, *40* (1), 53−61.

(29) Catalan, G.; Scott, J. F. *Adv. Mater.* **2009**, *21* (24), 2463−2485.

(30) Zavaliche, F.; Yang, S. Y.; Zhao, T.; Chu, Y. H.; Cruz, M. P.; Eom, C. B.; Ramesh, R. *Phase Transitions* **2006**, *79* (12), 991−1017.

(31) Christen, H. M.; Nam, J. H.; Kim, H. S.; Hatt, A. J.; Spaldin, N. A. *Phys. Rev. B: Condens. Matter Mater. Phys.* **2011**, *83* (14), 144107.

(32) Beekman, C.; Siemons, W.; Ward, T. Z.; Chi, M.; Howe, J.; Biegalski, M. D.; Balke, N.; Maksymovych, P.; Farrar, A. K.; Romero, J. B.; Gao, P.; Pan, X. Q.; Tenne, D. A.; Christen, H. M. *Adv. Mater.* **2013**, *25* (39), 5561−5567.

(33) Zeches, R. J.; Rossell, M. D.; Zhang, J. X.; Hatt, A. J.; He, Q.; Yang, C. H.; Kumar, A.; Wang, C. H.; Melville, A.; Adamo, C.; Sheng, G.; Chu, Y. H.; Ihlefeld, J. F.; Erni, R.; Ederer, C.; Gopalan, V.; Chen, L. Q.; Schlom, D. G.; Spaldin, N. A.; Martin, L. W.; Ramesh, R. *Science* **2009**, *326* (5955), 977−980.

(34) Dixit, H.; Beekman, C.; Schleputz, C. M.; Siemons, W.; Yang, Y.; Senabulya, N.; Clarke, R.; Chi, M. F.; Christen, H. M.; Cooper, V. R. *Adv. Sci.* **2015**, *2* (8), 1500041.

(35) Nelson, C. T.; Winchester, B.; Zhang, Y.; Kim, S. J.; Melville, A.; Adamo, C.; Folkman, C. M.; Baek, S. H.; Eom, C. B.; Schlom, D. G.; Chen, L. Q.; Pan, X. Q. *Nano Lett.* **2011**, *11* (2), 828−834.

(36) Li, L. Z.; Gao, P.; Nelson, C. T.; Jokisaari, J. R.; Zhang, Y.; Kim, S. J.; Melville, A.; Adamo, C.; Schlom, D. G.; Pan, X. Q. *Nano Lett.* **2013**, *13* (11), 5218−5223.

(37) Zhang, J. X.; Ke, X. X.; Gou, G. Y.; Seidel, J.; Xiang, B.; Yu, P.; Liang, W. I.; Minor, A. M.; Chu, Y. H.; Van Tendeloo, G.; Ren, X. B.; Ramesh, R. *Nat. Commun.* **2013**, *4*, 2768.

(38) Withers, R. L.; Thompson, J. G.; Rae, A. D. *J. Solid State Chem.* **1991**, *94* (2), 404−417.

(39) Liu, H. J.; Yang, P.; Yao, K.; Ong, K. P.; Wu, P.; Wang, J. *Adv. Funct. Mater.* **2012**, *22* (5), 937−942.

(40) Nelson, C. T.; Gao, P.; Jokisaari, J. R.; Heikes, C.; Adamo, C.; Melville, A.; Baek, S. H.; Folkman, C. M.; Winchester, B.; Gu, Y. J.; Liu, Y. M.; Zhang, K.; Wang, E. G.; Li, J. Y.; Chen, L. Q.; Eom, C. B.; Schlom, D. G.; Pan, X. Q. *Science* **2011**, *334* (6058), 968−971.

(41) Jeon, B. C.; Lee, D.; Lee, M. H.; Yang, S. M.; Chae, S. C.; Song, T. K.; Bu, S. D.; Chung, J. S.; Yoon, J. G.; Noh, T. W. *Adv. Mater.* **2013**, *25* (39), 5643.

(42) Beekman, C.; Siemons, W.; Chi, M.; Balke, N.; Howe, J. Y.; Ward, T. Z.; Maksymovych, P.; Budai, J. D.; Tischler, J. Z.; Xu, R.; Liu, W.; Christen, H. M. *Adv. Funct. Mater.* **2016**, *26* (28), 5166−5173.

DOI: 10.1021/acs.nanolett.7b00696
Nano Lett. 2017, 17, 3556−3562